Multi-component Evaporation of Sustainable Aviation Fuel Droplets

Poblador-Ibanez, Jordi; Nocivelli, Lorenzo; Dasgupta, Debolina

DOI
10.2514/6.2024-1997

Publication date
2024

Document Version
Final published version

Published in
AIAA SciTech Forum and Exposition, 2024

AIAA SciTech Forum
8-12 January 2024, Orlando, FL
AIAA SCITECH 2024 Forum

10.2514/6.2024-1997

Multi-component Evaporation of Sustainable Aviation Fuel Droplets

Jordi Poblador-Ibanez[1],
Delft University of Technology, Delft, 2628 CD, The Netherlands
Argonne National Laboratory, Lemont, IL, 60439, United States

Lorenzo Nocivelli[2], and Debolina Dasgupta[3]
Argonne National Laboratory, Lemont, IL, 60439, United States

Sustainable Aviation Fuels (SAF) will gradually replace current fossil fuels (e.g., Jet A) over the next few decades to achieve the decarbonization goals of the aviation industry by 2050. Despite efforts to design drop-in biofuels which meet specific fuel property requirements, uncertainties remain on the fuel behavior across the engine operating range. Typical chemical pathways to produce SAF result in simpler composition spectrums with potentially few mixture components. Thus, preferential evaporation may become important and affect the evaporation and subsequent combustion characteristics. Currently available experimental data focusing on Category C biofuels (i.e., SAF) from the National Jet Fuels Combustion Program (NJFCP) already shows preferential evaporation effects on the fuel distillation curve at atmospheric pressure. In this study, a computational framework based on a real-fluid thermophysical model is used to analyze the evaporation of Category C fuel droplets at various combustion chamber operating conditions. This includes low pressure – low temperature conditions (e.g., start-up, idle) and high pressure – high temperature environments (e.g., cruise, take-off).

I. Nomenclature

a	=	molecular attraction parameter in the equation of state
b	=	volumetric parameter in the equation of state
c	=	volumetric correction in the equation of state
c_p	=	isobaric specific heat
D	=	Fickian mass diffusion coefficient
d	=	droplet diameter
d0	=	initial droplet diameter
f	=	fugacity
h	=	enthalpy
J	=	radial mass flux
k_{ij}	=	binary interaction coefficient in the equation of state
M	=	molecular weight
$\dot{m}$	=	net mass flux per unit area across the interface
N	=	number of species in the mixture
p	=	pressure
R_u	=	universal gas constant 8.31446 J/(mol*K)
r	=	radial coordinate
T	=	temperature
t	=	time

[1] Postdoctoral Researcher, Department of Maritime and Transport Technology (Delft University of Technology) and Transportation and Power Systems Division (Argonne National Laboratory), AIAA Young Professional Member.
[2] Research Scientist, Transportation and Power Systems Division, AIAA Young Professional Member.
[3] Research Scientist, Transportation and Power Systems Division, AIAA Young Professional Member.

u = radial velocity
$\bar{v}$ = molar volume
X = mole fraction
Y = mass fraction
Z = compressibility factor $Z = p\bar{v}/(R_u T)$

Greek Symbols
α = thermal diffusivity
Γ = thermodynamic factor
λ = thermal conductivity
ρ = density
Φ = fugacity coefficient
ω = molecular acentric factor

Subscripts
c = critical point value
g = relative to the gas phase
i or j = relative to species i or j
l = relative to the liquid phase

II. Introduction

The aviation industry, in the United States, currently contributes to more than 10% of the greenhouse gas (GHG) emissions from transportation[4] and regulatory agencies are setting clear goals for its decarbonization by 2050. However, the technology mix defined to win this challenge is strongly different from the ground transportation sector. In fact, despite its rapid and broad implementation in light-duty ground vehicles, electrification or hydrogen-based technologies are a promising solution only for small aircraft operating at short-medium range (e.g., Airbus ZEROe project[5]), and remain very limited for long-haul airplanes. Consequently, the introduction of renewable sources to produce jet fuels to replace fossil-based kerosene (e.g., Jet A), which allow net-zero carbon emissions during their life cycle, could play a pivotal role in the reduction of the aviation sector's GHG emissions.

Given the extensive testing required to certify new fuels, government- and industry-backed research programs, e.g., National Jet Fuels Combustion Program (NJFCP) [1], established methods to pre-screen sustainable aviation fuel (SAF) candidates, assessing and defining their thermophysical and reacting characteristics and highlighting the differences in their behavior compared with conventional fossil fuels.

Computational Fluid Dynamics (CFD) is a well-established tool to de-risk the design and implementation of new technologies and it will play a relevant role in the assessment of the performance of SAF in realistic engine operations. With the constant increase in computational power, simulations are now capable of capturing the complete injection and combustion processes on full scale systems, and have been recently used to assess the sensitivity of the lean blow-out to modifications of the fuel properties [2]. The definition and implementation of accurate models to describe the real fluid behavior is therefore instrumental for the simulation of the multi-phase and reacting characteristics of the engine. Moreover, their integration with CFD platforms requires computational affordability and flexibility.

Some of the proposed SAF surrogates, namely Category C or C-type fuels, have been characterized experimentally [3,4]. They report fuel compositions with a limited number of hydrocarbons (including n-paraffins, iso-paraffins, and cyclo-alkanes) and their composition spectrums are therefore narrower when compared with the typical complex mixture characteristics of Jet A/A-1. This characteristic enables the introduction of detailed frameworks to calculate the thermophysical properties of the SAF, going beyond the common practice established for traditional fossil-based jet fuels, which is based on the use of single component surrogates, such as n-dodecane to represent Jet A [5], or constant properties [6].

A real fluid model (RFM) approach, based on efficient algebraic cubic equations of state (EoS) coupled with basic thermodynamic principles and correlations to estimate the fluid and transport properties [7,8], therefore becomes very appealing to be integrated in CFD frameworks. Given the operating conditions of the engine, which range from low

[4] Sustainable Aviation Fuel (SAF) Grand Challenge Roadmap, U.S. Department of Energy. Source: https://www.energy.gov/eere/bioenergy/articles/sustainable-aviation-fuel-grand-challenge-roadmap-flight-plan-sustainable
[5] Airbus ZEROe project. Source: https://www.airbus.com/en/innovation/low-carbon-aviation

pressure (0.4 bar) and temperatures (<250K) for high-altitude relight to supercritical pressures (60 bar) and temperatures (>1000 K) for take-off conditions [1], the RFM needs to capture non-idealities of multi-component fluids, as shown for in rocket engines or heavy-duty diesel-type engines [9-12].

This work presents the application of the RFM, which has been developed and validated against data for Category C SAF surrogates in its prediction of the thermophysical properties and vapor-liquid-equilibrium (VLE) dynamics [7,8], to the simulation of a single vaporizing droplet in quiescent conditions, aiming at assessing the characteristics of multi-component dynamics of different SAF and at establishing a first step towards its implementation in a comprehensive CFD software. This work pursues the definition of a high-fidelity approach for the modeling of the multi-component vaporization process at various engine operating regimes, which extends beyond simplified approaches as continuous thermodynamics models (CTM) [13-16] or distillation curve methods [17].

This manuscript presents the following: (i) RFM approach, (ii) numerical framework and assumptions, (iii) validation against experimental data from literature, and (iv) assessment of the multi-component droplet evaporation of Category C fuels at different operating conditions.

III. Modeling

This section introduces the governing equations (Section III.A), the thermophysical model (Section III.B), and the numerical approach (Section III.C) to solve the vaporizing multi-component droplet in a quiescent environment. Although more detailed features may be included in the future (e.g., convective stream, recirculation inside the droplet), this study represents a first step toward understanding multi-component evaporation of SAF droplets at relevant operating conditions described in Section III.D.

A. Governing Equations

For a vaporizing droplet suspended in a quiescent environment, the governing equations have been simplified with the following assumptions: (a) spherical symmetry, (b) constant ambient pressure, (c) negligible thermo-diffusion (i.e., Soret effect), (d) negligible radiative heat transfer, (e) negligible viscous dissipation, (f) negligible gravity effects, and (g) non-reacting flow. As a result, the momentum equation does not need to be solved and the radial velocity is directly obtained from the continuity equation. Although various works addressing droplet evaporation include the radial momentum equation for completeness [18,19], it may be neglected if the momentum flux is substantially smaller than the ambient pressure and the problem is diffusion driven [20,21]. This assumption is validated using a high-fidelity two-phase solver in a similar non-spherical one-dimensional configuration for pressures as low as 10 bar [22].

The governing equations are the continuity, species transport and energy equations, given by

$$\frac{\partial \rho}{\partial t} + \frac{1}{r^2}\frac{\partial}{\partial r}(\rho r^2 u) = 0 \tag{1}$$

$$\frac{\partial \rho Y_i}{\partial t} + \frac{1}{r^2}\frac{\partial}{\partial r}(\rho Y_i r^2 u) = -\frac{1}{r^2}\frac{\partial}{\partial r}(r^2 J_i) \tag{2}$$

$$\frac{\partial \rho h}{\partial t} + \frac{1}{r^2}\frac{\partial}{\partial r}(\rho h r^2 u) = \frac{1}{r^2}\frac{\partial}{\partial r}\left(r^2 \frac{\lambda}{c_p}\frac{\partial h}{\partial r}\right) - \sum_{i=1}^{N}\frac{1}{r^2}\frac{\partial}{\partial r}\left(r^2 h_i \left[J_i + \frac{\lambda}{c_p}\frac{\partial Y_i}{\partial r}\right]\right) \tag{3}$$

Note that the energy equation has been rewritten in terms of the mixture enthalpy and the transformation $\lambda \nabla T = (\lambda/c_p)\nabla h - \sum_{i=1}^{N}(\lambda/c_p)h_i \nabla Y_i$ has been used. The diffusion mass fluxes J_i originate from the generalized Maxwell-Stefan equations [19] and, neglecting thermo-diffusion, can be rewritten in terms of Fickian diffusion fluxes as $\boldsymbol{J} = -\rho \boldsymbol{D} \boldsymbol{\nabla Y}$ [23], where $\boldsymbol{J}$ and $\boldsymbol{\nabla Y}$ are vectors of size N-1 including the diffusive mass flux and radial composition gradients, respectively. That is, the condition of zero net flux is imposed ($\sum_{i=1}^{N} J_i = 0$). In this work, only N-1 species transport equations are solved and $Y_N = 1 - \sum_{i=1}^{N-1} Y_i$. $\boldsymbol{D}$ is a square matrix of size N-1 representing Fickian diffusion coefficients obtained from Maxwell-Stefan binary diffusion coefficients and non-ideal thermodynamic factors Γ [23,24]. Γ can be obtained from the fugacity of the mixture components and captures non-ideal diffusion behaviors, such as the reversed diffusion process (unstable system) linked to phase separation and the emergence of transcritical interfaces [25].

The interface between liquid and gas is treated as a sharp contact discontinuity with negligible thickness. Therefore, jump conditions or interface conservation relations must be satisfied. An interface undergoing phase change

propagates relative to the fluid at a radial velocity u_{int}. Thus, the conservation relations across (normal to) the interface for Eqs. (1) to (3) are given by

$$\dot{m} = \rho_g(u_g - u_{int}) = \rho_l(u_l - u_{int}) \tag{4}$$

$$\rho_g Y_{g,i}(u_g - u_{int}) + J_{g,i} = \rho_l Y_{l,i}(u_l - u_{int}) + J_{l,i} \tag{5}$$

$$\rho_g h_g(u_g - u_{int}) - \left(\frac{\lambda}{c_p}\frac{\partial h}{\partial r}\right)_g + \sum_{i=1}^{N}\left(h_i\left[J_i + \frac{\lambda}{c_p}\frac{\partial Y_i}{\partial r}\right]\right)_g = \rho_l h_l(u_l - u_{int}) - \left(\frac{\lambda}{c_p}\frac{\partial h}{\partial r}\right)_l + \sum_{i=1}^{N}\left(h_i\left[J_i + \frac{\lambda}{c_p}\frac{\partial Y_i}{\partial r}\right]\right)_l \tag{6}$$

Eq. (4) can be rearranged to express the velocity jump across the interface as a function of $\dot{m}$ as $(u_g - u_l) = \left(\frac{1}{\rho_g} - \frac{1}{\rho_l}\right)\dot{m}$. Thus, under no phase change, the interface is just advected with the fluid. Moreover, substitution of Eq. (4) into Eqs. (5) and (6) yields more compact equations in terms of $\dot{m}$.

A thermodynamic closure for the interface is given by the assumption that the interface is locally under vapor-liquid equilibrium conditions [18-22]. Equilibrium for real-fluid conditions is expressed in terms of an equality of the fugacity of each component across the interface $f_{g,i} = f_{l,i}$, where fugacity takes the role of an effective partial pressure [26]. Rearranging in terms of the fugacity coefficient, the equilibrium condition is expressed as $p_g X_{g,i}\Phi_{g,i} = p_l X_{l,i}\Phi_{l,i}$. Clearly, the equilibrium condition depends on the pressure on both sides of the interface, while Φ depends on pressure, temperature, and composition. To further simplify the VLE problem, temperature is assumed to be continuous (i.e., $T_g = T_l$) and the constant-pressure assumption discussed earlier holds (i.e., $p_g = p_l$). However, a pressure jump would still exist across the interface due to interfacial surface tension and momentum exchange due to phase change. Note the contribution of the differences in normal viscous stresses is neglected. Nonetheless, the pressure discontinuity is negligible for phase equilibrium purposes [21]. The validity of the interfacial treatment described in previous lines has been previously discussed under similar target conditions as those from this work [22]. However, note that this interface treatment does not consider the transition of the mixture to a supercritical state, nor the possibility that non-equilibrium interfacial dynamics (e.g., solving the interface state via linear gradient theory) may offer more accurate predictions of transcritical interfaces under certain conditions [25].

B. Thermophysical Modeling

A real-fluid model is used to represent the fluid properties of each phase and the transition from liquid to gas. It is built on three key cornerstones, namely the equation of state, the coupling with generalized correlations to obtain fluid properties, and the VLE assumption to represent the phase boundary. The details on the RFM framework are available in Poblador-Ibanez and Nocivelli [8], where validation against reference data is also shown. The NIST[6] Webbook[7] and NIST REFPROP[8] have been used to validate the model for well-known individual components (e.g., n-dodecane) and hydrocarbon mixtures relevant to SAF using different cubic equations of state. Moreover, the performance of the RFM has been evaluated in the same work against available SAF experimental data from Edwards [3] and Boehm et al. [4] using fuel surrogates, which is further discussed in Section IV.B. In the present work, a summary of the RFM is provided.

A volume-translated Soave-Redlich-Kwong cubic equation of state (VT-SRK EoS) [27] is used in the present RFM framework based on the observed accuracy in the conditions of interest [8]. Due to the two-parameter nature of the original SRK EoS, a volumetric correction is needed to improve the density prediction of dense fluids (e.g., liquids) and related properties that are obtained via generalized correlations which depend on the fluid density. In particular, the generalized multiparameter correlation by Chung et al. [28] is used to estimate viscosity and thermal conductivity, while diffusion mass fluxes are obtained from the unified model for non-ideal multicomponent molecular diffusivity by Leahy-Dios and Firoozabadi [23]. If needed, the surface tension coefficient can be estimated from the Macleod-Sugden correlation [26,29], which also depends on the density calculations.

[6] National Institute of Standards and Technology, U.S. Department of Commerce
[7] https://webbook.nist.gov/
[8] Reference Fluid Thermodynamic and Transport Properties Database

$$p = \frac{R_u T}{\bar{v} + c - b} - \frac{a}{(\bar{v} + c + b)(\bar{v} + c)} \tag{7}$$

$$a = \sum_{i=1}^{N}\sum_{j=1}^{N} X_i X_j \left(a_i a_j\right)^{0.5}\left(1 - k_{ij}\right) \qquad b = \sum_{i=1}^{N} X_i b_i \qquad c = \sum_{i=1}^{N} X_i c_i \tag{8}$$

The VT-SRK EoS is given by Eq. (7), with quadratic and linear mixing rules being used for the EoS parameters (see Eq. (8)) described in [27]. Different mixing rules can be adopted in the other models and correlations integrated into the RFM [23,26,28,29]. Note the inclusion of binary interaction coefficients in the quadratic mixing rule of the molecular attraction parameter a. In general, this coefficient is not zero and is obtained by fitting the EoS results with experimental VLE data. Despite efforts to develop generalized methods to estimate k_{ij} [30], a comprehensive model cannot address the broad range of components involved in SAF. For hydrocarbon blends, $k_{ij} \approx 0$. However, a value ranging from 0.1 to 0.2 might be necessary to increase the accuracy of mixtures of hydrocarbons with air components or combustion products. In this work, $k_{ij} = 0$ pending new experimental data, if not explicitly specified. Additionally, the properties required to evaluate a, b, and c might not be readily available for some SAF components (e.g., iso-paraffins). Then, the critical point (p_c, T_c, ρ_c) and the molecular acentric factor are estimated from group contribution methods [31,32].

The EoS can be used to calculate derived thermodynamic properties using the concept of departure functions [26]. The mixture enthalpy is obtained from Eq. (9), where h^* represents the ideal-gas mixture enthalpy. h^* is obtained from the ideal-gas isobaric specific heat as $h^* = h_{ref} + \int_{T_{ref}}^{T} c_p^* \, dT$, where $h_{ref} = 0$ at $T_{ref} = 298$ K. c_p^* is obtained from generalized correlations and ideal-gas mixing rules, which is based on a group contribution strategy depending on the component [33,34]. Then, c_p and the species partial enthalpy h_i can be obtained by differentiation following fundamental thermodynamic principles. Similarly, Φ_i is obtained from Eq. (10). More details on the RFM based on the VT-SRK EoS are available in previous works [8,35].

$$h = h^* + \frac{R_u T}{M}\left[(Z - 1) + \int_{\infty}^{\bar{v}} T\left(\frac{\partial Z}{\partial T}\right)_{\bar{v},X_i} \frac{d\bar{v}}{\bar{v}}\right] \tag{9}$$

$$\ln(\Phi_i) = \int_{\infty}^{\bar{v}} \left(\frac{1}{\bar{v}} - \frac{1}{R_u T}\left(\frac{\partial p}{\partial X_i}\right)_{T,\bar{v},X_{j\neq i}}\right) d\bar{v} - \ln(Z) \tag{10}$$

C. Numerical Approach

A numerical treatment similar to those described in previous literature [18-21] is considered. The set of governing equations presented in Section III.A is solved with a time-marching scheme. First, the species composition and mixture enthalpy are updated by solving the non-conservative form of Eqs. (2) and (3) with a first-order explicit temporal scheme. Then, the new temperature and fluid properties are obtained from the thermophysical model. Next, the continuity equation determines the velocity field based on the temporal and spatial density variations. Lastly, the new interface state is calculated and the phase front advanced by solving the coupled system of equations given by Eqs. (4) to (6) and VLE (i.e., fugacity relations). The governing equations are discretized in a uniform mesh of spacing Δr with the interface moving according to the solution of the system of equations. The boundary conditions at $r = 0$ are $u = 0$, $\partial Y_i/\partial r = 0$, and $\partial h/\partial r = 0$, while the boundary conditions at $r \to \infty$ are $Y_i = Y_{g,\infty}$ and $h = h_{g,\infty}$. Numerically, the external boundary is set sufficiently far away from the droplet's surface (in this work, $r_\infty = 10 d_{drop}$ for all simulations), but $\partial Y_i/\partial r|_\infty = 0$ and $\partial h/\partial r|_\infty = 0$ are used in case the mixing layers reach the external boundary. Negligible differences are observed in the droplet dynamics when choosing one boundary condition over the other. A variable time step Δt is implemented given by $\Delta t = \mathrm{CFL} \times \min(\Delta t_u, \Delta t_Y, \Delta t_h, \Delta t_{int})$, where $\Delta t_u^{-1} = \max(|u|)/\Delta r$, $\Delta t_Y^{-1} = \max(\boldsymbol{D})/\Delta r^2$, $\Delta t_h^{-1} = \max(\lambda/(\rho c_p))/\Delta r^2$ and $\Delta t_{int}^{-1} = |u_{int}|/\Delta r$. After preliminary tests, $\mathrm{CFL} = 0.2$ is set for this study.

For discretization purposes, the velocity and diffusion mass fluxes are staggered with respect to all other variables in a cell center/cell faces configuration. Away from the interface, second-order finite difference schemes (e.g., central differences) are used to discretize both convective and diffusive terms. The flow velocities arising from the Stefan

flow and the thermal expansion of the droplets coupled to the dissolution of lighter components are sufficiently small to justify the use of central differences. In the two cells separated by the interface, the interface solution is directly embedded in the discretization schemes. For the convective terms of the species and energy transport equations, the cell-centered velocity results from the average between the respective phase-wise velocity at the interface (u_g or u_l) and the velocity at the opposite face. Similarly, the interface solution of the respective phase is used to calculate the composition and enthalpy gradients at the cell center. In the continuity equation, the interface density is used in the discretized convective term to calculate the phase-wise velocity at the interface. The discretized diffusive terms include the interface solution in a similar manner and use the interface properties and location when needed. However, the composition and enthalpy gradients in the discretization scheme corresponding to the interface side are replaced by one-sided second-order gradients calculated by means of a normal probe technique. That is, two points are defined on each side of the interface at a distance of Δr and $2\Delta r$, respectively. Then, composition and enthalpy values are interpolated onto these points and, together with the interface value, one-sided finite differences are used. The probing method is chosen instead of calculating one-sided gradients directly from the values stored at the interface and neighboring nodes to avoid dealing with singularities arising from the interface approaching a grid node. The spatial accuracy near the interface is second order at best when the interface coincides with a cell face or the midpoint between two nodes but deteriorates to first order when the interface approaches a node.

By substituting Eq. (4) into Eqs. (5) and (6), the interface state is determined by a $2N + 2$ system of equations given by $N - 1$ species conservation relations (i.e., summation of Eq. (5) from $i = 1$ to N results in Eq. (4)), N fugacity relations, the energy conservation relation Eq. (6), $\sum_{i=1}^{N} X_{g,i} = 1$ and $\sum_{i=1}^{N} X_{l,i} = 1$. The solution of this system of equations is the mixture composition on either side of the interface ($2N$ variables), the interface temperature and the mass flux $\dot{m}$. Note that the normal probe technique is also used here to evaluate one-sided gradients with second-order accuracy. The interface location, r_{drop}, is updated as $r_{drop}^{n+1} = r_{drop}^{n} + u_{int}^{n+1}\Delta t$, with the interface velocity evaluated as $u_{int} = u_l - \dot{m}/\rho_l$. Following the approach by He and Ghoniem [19], the node values are updated by the respective interface values if the interface moves across it. For example, if a node initially belongs to the liquid phase, it is then updated with the interface solution on the gas side as the diameter of the droplet changes. These node updates may introduce some oscillations in the interface properties trends with time but disappear with mesh refinement and are not detrimental to numerical stability.

D. Target Conditions

Representative ambient conditions for the droplets may vary significantly depending on the operating condition of the engine across the flight envelope and the location of the droplet within the spray. Atomizers used in jet engine combustors include swirlers to enhance atomization and stabilize the flame, which result in the appearance of two distinct recirculation zones, namely the outer recirculation zone (ORZ) and the central recirculation zone (CRZ) [1]. These two regions tend to show different gas properties, with the CRZ carrying hotter gases with a lower oxygen concentration upstream [2,36,37]. The ORZ typically has lower temperatures and a higher oxygen concentration compared to the CRZ. As such, three different operating environments are considered where a deeper understanding of the multi-component nature of SAF is required: lean blowout (LBO), cruise, and take-off. Based on previous literature [1,2,36,37], the temperature, pressure, and gas composition for target conditions representative of these three operating regimes (e.g., p_3 and T_3 conditions) are reported in Table 1. Note that the CRZ is assumed to carry no combustion products for this study, and that relatively high operating pressures are considered at cruise and take-off conditions, following current engine development trends.

Table 1 Target conditions for the multi-component droplet evaporation study.

Operating Regime	d_{drop} (μm)	T_{drop} (K)	p (bar)	Zone	$T_{g,\infty}$ (K)	$X_{O_2,\infty}$	$X_{N_2,\infty}$
LBO	30	310	3.3	ORZ	450	0.21	0.79
				CRZ	900	0.15	0.85
Cruise	20	363	20	ORZ	800	0.21	0.79
				CRZ	1200	0.15	0.85
Take-off	5	363	60	ORZ	900	0.21	0.79
				CRZ	1200	0.15	0.85

The initial conditions for the droplet temperature and diameter follow additional assumptions. Although the results may be compared using non-dimensional scalings, this work aims to start from relevant physical parameters and scales. Note that the droplet initial temperature is uncertain and can be dependent on the heat transfer across the atomizer and the liquid phase heating during the atomization process at different conditions. Nonetheless, the choice of a possibly low temperature allows for sufficient heating of the droplet to observe preferential evaporation effects and relevant transcritical features at high pressures. For LBO conditions, the droplet is initialized at 310 K, which corresponds to a typical expected injected fuel temperature [1]. The initial droplet diameter is obtained from experimental observations at low pressure conditions (e.g., LBO, atmospheric pressure). Experimental works show typical droplet diameters are of the order of $\mathcal{O}(10\ \mu\text{m})$ for relevant aviation fuels injected with swirl-assisted atomizers [38-41]; thus, 30 μm has been chosen as a representative value. For cruise and take-off conditions, a higher droplet temperature of 363 K is considered. This value is chosen based on fuel temperature assumptions in diesel-like injectors at the high-temperature and high-pressure conditions of 900 K and 60 bar [12]. However, transcritical conditions result in a wider temperature range of two-phase coexistence and much hotter droplets may be observed [25]. Regarding the droplet diameter, an educated guess needs to be made. The high chamber pressures representative of cruise and take-off conditions result in a much denser air flow and the dissolution of ambient gas species into the liquid fuel mixture. As a result, the atomization of the fuel is enhanced due to the increased gas inertia and variations in the liquid properties such as decreased density, viscosity, and surface tension [42]. Experimental results up to a chamber pressure of 7 bar already show this trend [43], although at these mild pressures the increased gas density is the major contribution to the diameter reduction. Given the uncertainties and the lack of relevant experimental and computational data at these conditions, the initial droplet diameters are set to 20 μm at cruise and 5 μm at take-off. These droplet parameters are also included in Table 1.

IV. Results

This section presents the results obtained with the RFM and the droplet model. First, Section IV.A describes the Category C fuel surrogates used in this study, followed by their characterization using the RFM and the relevant features of their distillation curve (Section IV.B) and the vapor-liquid equilibrium with air (Section IV.C). Then, the droplet model is validated for a binary mixture in Section IV.D. Lastly, Section IV.E discusses the droplet evaporation characteristics of the Category C fuel surrogates.

A. Category C Fuel Surrogates

Four different fuel surrogate mixtures representing Category C biofuels (i.e., SAF candidates) from the NJFCP are analyzed in this work (C-1 or POSF# 13718, C-2 or POSF# 12223, and C-5 or POSF# 12345). The detailed composition of these fuels can be found in Edwards [3] and in the Alternative Jet Fuel Test Database[9] (AJFTD). Figure 1 shows the composition (by mass) of the fuel surrogates. Note that a binary surrogate for C-1 is also considered, named hereinafter C-1ez, as it is commonly used in the literature [44]. Nonetheless, the need for a more detailed composition for C-1 becomes evident, especially to capture the fuel distillation trends and preferential evaporation [7,8] (see Section IV.B). The choice of fuels covers a range of features: (a) iso-paraffinic blends (C-1), (b) bimodal behaviors (C-1 and C-2), (c) fuel blends containing aromatic compounds (C-2 and C-5), and (d) fuels exhibiting extremely flat boiling behaviors (C-5).

The iso-paraffins considered in this work have been defined based on previous literature and component availability [3,44-46] and include iso-decane or 3,6-dimethyl octane (iC10), iso-undecane or 2,5,6-trimethyl octane (iC11), iso-dodecane or 2,2,4,6,6-pentamethyl heptane (iC12), iso-tridecane or 2,2,9-trimethyl decane (iC13), iso-tetradecane or 2,3,5,8-tetramethyl decane (iC14), iso-hexadecane or 2,2,4,4,6,8,8-heptamethyl nonane (iC16), and iso-icosane or 2,2,4,4,6,6,8,8,10-nonamethyl undecane (iC20). Moreover, the surrogates may include normal paraffins such as n-decane (nC10), n-dodecane (nC12), and n-tetradecane (nC14), and the aromatic compound mesitylene or 1,3,5-trimethyl benzene (bM3). Table 2 shows the relevant physical properties of these hydrocarbons, as well as nitrogen (N_2) and oxygen (O_2), necessary for the RFM.

[9] https://altjetfuels.illinois.edu/

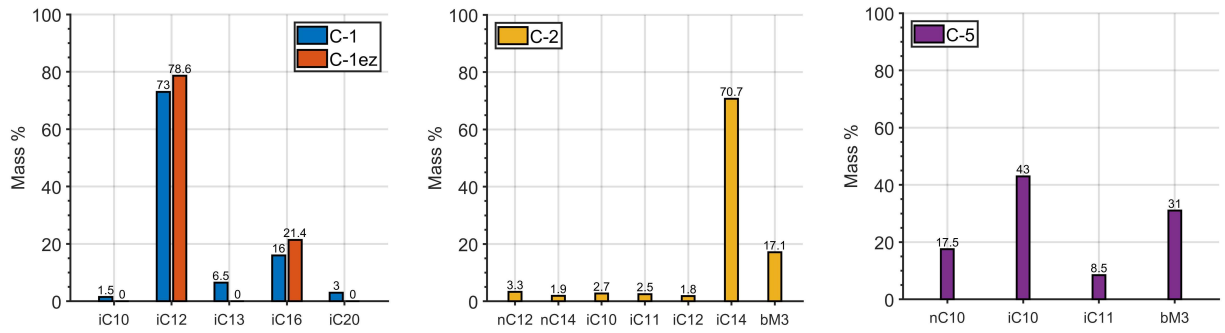

Fig. 2 Composition in terms of mass percentage of the Category C fuel surrogates C-1 (POSF# 13718), the binary surrogate C-1ez, C-2 (POSF# 12223), and C-5 (POSF# 12345).

Table 2 Physical properties of the species considered in this work, including molecular weight, critical point, and acentric factor. The data is obtained from the NIST Webbook, the NIST REFPROP software, and the references discussed in Section III.B.

Species	M (g/mol)	T_b (K)	T_c (K)	p_c (bar)	ρ_c (kg/m^3)	ω
N_2	28.01	77.36	126.19	33.96	313.30	0.0372
O_2	32.00	90.19	154.58	50.43	436.14	0.0222
nC10	142.28	447.27	617.70	21.03	233.34	0.4884
nC12	170.33	489.30	658.10	18.17	226.55	0.5740
nC14	198.39	523.00	693.00	16.00	221.91	0.6648
iC10	142.28	433.00	605.07	21.52	235.41	0.4842
iC11	156.31	451.00	627.34	20.44	238.03	0.4925
iC12	170.33	451.00	628.62	19.50	240.76	0.4283
iC13	184.36	486.00	660.08	17.53	231.91	0.5377
iC14	198.39	518.16	695.89	16.30	231.29	0.5736
iC16	226.44	513.20	692.00	15.70	233.47	0.5345
iC20	282.55	643.84	836.51	11.90	226.45	0.6238
bM3	120.19	437.80	639.00	31.30	274.76	0.3780

B. Characterization of Sustainable Aviation Fuels

A limited amount of validation data for SAF exists at atmospheric pressure conditions (i.e., 1 bar) and relatively low temperatures. Some sources are Edwards [3] and Boehm et al. [4] and include experimental values of select properties of Category C fuels. A thorough validation of the RFM has been previously performed for SAF in the broad range of operating conditions [7,8]. Thus, this section only shows the trends of relevant properties of the considered fuel surrogates from Fig. 1. Figure 2 presents a comparison between the RFM and the experimental data for density and specific heat at constant pressure at 1 bar. In general, good agreement is observed, especially at temperatures above 300 K corresponding to the target conditions from Table 1. However, deviations from the reference data occur at lower temperatures that require further model improvements.

Figure 3a illustrates the distillation curve of the Category C fuel surrogates obtained using a pT flash solver based on the fugacity relations and the Rachford-Rice equation [47], which imposes mass conservation in a homogeneous mixture of vapor and liquid in equilibrium. Note that the distillation of the liquid mixture is represented in terms of a vapor fraction of the mass conservation relations rather than a distilled volume percentage. A comparison against experimental data shows a remarkably good agreement in the distillation trends. For example, the flat boiling of C-5 is captured at a nearly constant temperature of 438 K, while the two different bimodal behaviors of C-1 and C-2 are

also represented [3]. However, larger differences exist for these two fuels regarding the starting and ending temperatures of the fuel boiling when compared to the experiments. Here, the RFM displays a strong sensitivity to the selected surrogate compositions, and care is needed when neglecting components due to their small concentration in the actual fuel. Although seemingly reasonable, the impact on the distillation curve and multi-component evaporation trends can be significant. This is illustrated when looking at C-1 and C-1ez. Though no major differences are observed in ρ and c_p, both fuels display different distillation curves as the vapor fraction increases, with C-1 approaching the experimental data better. The reason behind this difference is the inclusion of lower volatility components in the surrogate mixture that require higher temperatures toward the end of the distillation curve to vaporize. In this case, the 3% mass concentration of iC20 is the lower volatility component. Similarly, the experimental data shows lower temperatures at the start of boiling, which would be captured by the RFM if higher volatility components, in rather small concentrations, were included in the surrogate mixtures. These observations challenge the binary assumption for C-1 used in the literature if the distillation curve is to be captured accurately. More details on this and the impact on fluid properties across the distillation range are provided in Poblador-Ibanez and Nocivelli [8].

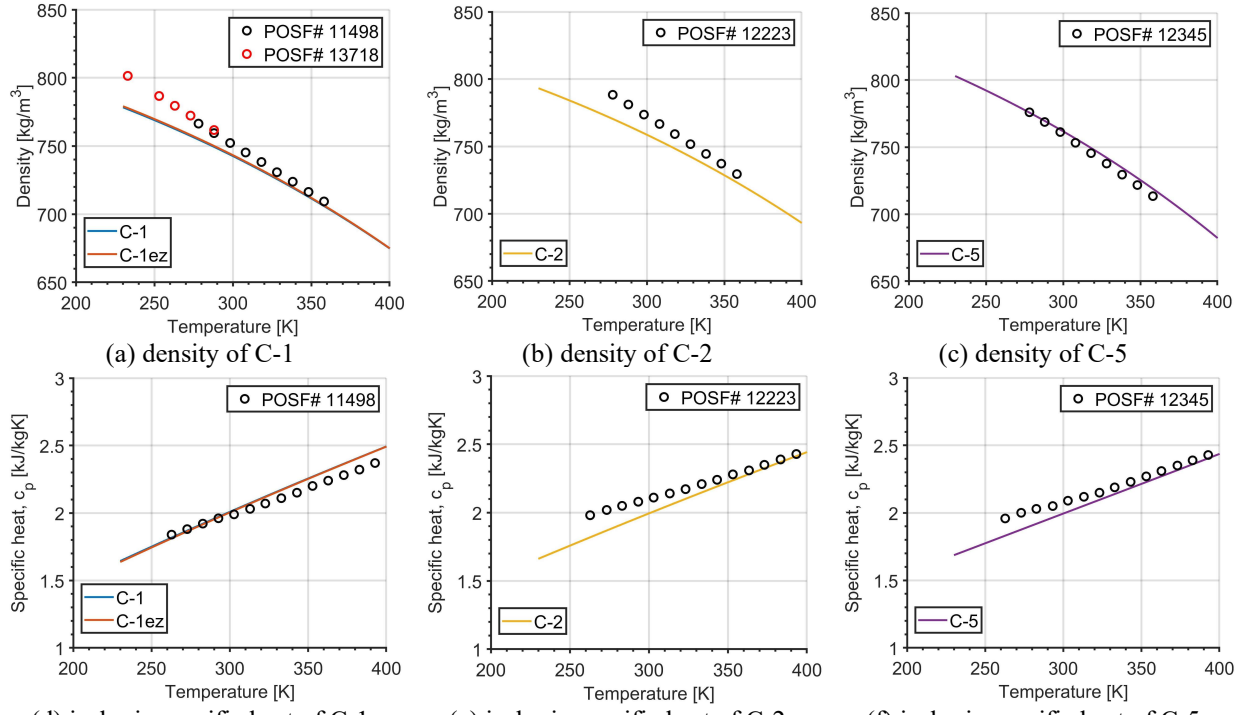

(a) density of C-1 (b) density of C-2 (c) density of C-5

(d) isobaric specific heat of C-1 (e) isobaric specific heat of C-2 (f) isobaric specific heat of C-5

Fig. 2 Liquid-phase properties of the Category C fuel surrogates at 1 bar. Results are compared against experimental data from Edwards [3] (POSF# 11498, 12223, and 12345) and Boehm et al. [4] (POSF# 13718). (a)-(c) density; (d)-(f) isobaric specific heat.

The saturation curves (i.e., bubble and dew lines) for the Category C fuel surrogates are shown in Fig. 3b. Vapor pressure trends agree with available experimental data in the temperature range of 300 K to 400 K [3], while the different temperature boiling range between C-1 and C-1ez is observed up to the critical point of each surrogate. Although direct methods exist to calculate the critical point of a mixture with a cubic EoS [48], an indirect method is used following the saturation curves. As a result, estimates of the critical point of SAF can be obtained from the RFM. The calculated critical pressures and temperatures of the surrogates are $p_c = 19.88$ bar and $T_c = 649.2$ K for C-1, $p_c = 19.26$ bar and $T_c = 642.5$ K for C-1ez, $p_c = 20.06$ bar and $T_c = 678.7$ K for C-2, $p_c = 22.76$ bar and $T_c = 613.3$ K for C-5. For reference, the critical point of Jet A has been estimated (in an average sense) to be $p_c = 23.81$ bar and $T_c = 671.15$K [49]. Thus, transcritical conditions occur at lower pressures and the effects are stronger for SAF when compared to current aviation fuel. For example, some SAF might exhibit transcritical behavior at cruise operation while Jet A does not.

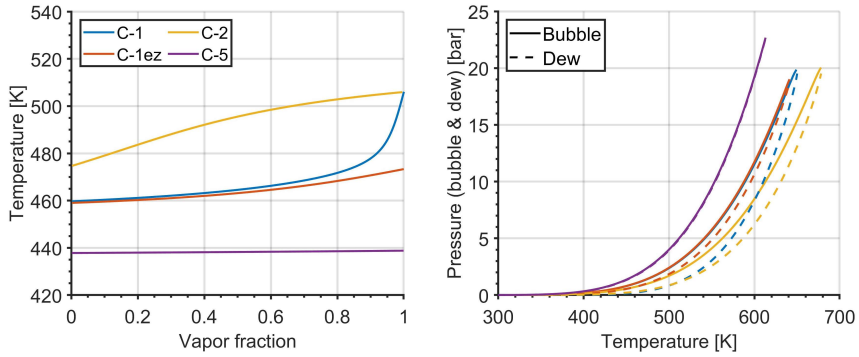

(a) distillation curves at 1 bar (b) bubble and dew lines

Fig. 3 Distillation curves at 1 bar and saturation pressure along the bubble and dew lines of the Category C fuel surrogates. (a) distillation curves at 1 bar; (b) bubble and dew lines.

Lastly, Fig. 4 shows the density, isobaric specific heat, and thermal conductivity of C-1 obtained with the RFM. The three pressure levels presented in Table 1 are considered, with the temperature ranging from 300 K to 1200 K. Note that the mixture two-phase region is highlighted at 3.3 bar. The capability of the RFM to extend SAF characterization beyond the available experimental data becomes immediately clear. The changes in liquid and vapor properties across the two-phase region and the strong non-linearities in the vicinity of the critical point (i.e., sharp density gradient, peak in isobaric specific heat) can be represented. C-1ez, C-2, and C-5 exhibit similar features and properties, but are affected by the different critical points (e.g., C-5 shows a very narrow two-phase region at 20 bar). The differences between Category C fuels at each operating condition are highlighted in the droplet evaporation study.

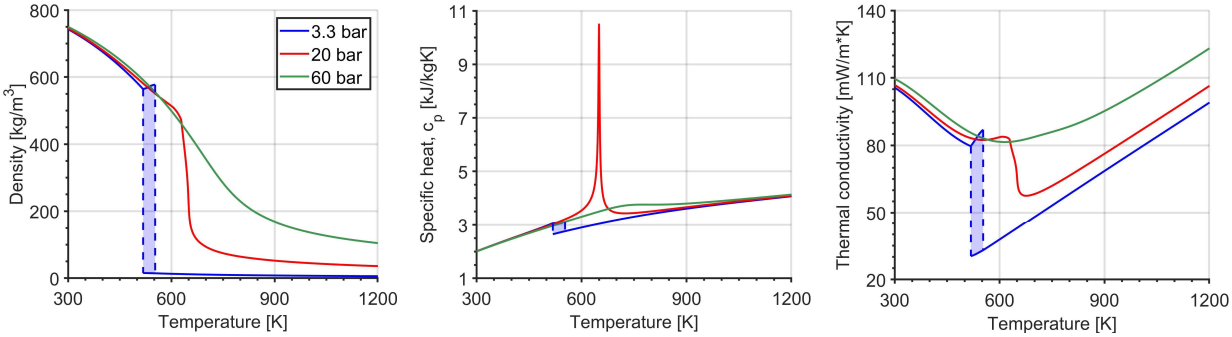

(a) density (b) isobaric specific heat (c) thermal conductivity

Fig. 4 Properties of the Category C fuel surrogate C-1 at different target conditions. The mixture two-phase region at 3.3 bar is shaded in blue. (a) density; (b) isobaric specific heat; (c) thermal conductivity.

C. Vapor-Liquid Equilibrium with Air

Section IV.B has discussed the features of the surrogate mixtures presented in Fig. 1. However, this work focuses on realistic configurations where the fuel is in contact with an ambient gas (i.e., air) and, as a result, the VLE characteristics are different [8]. For validation purposes, Fig. 5 shows the density, isobaric specific heat, and thermal conductivity of air (79% vol. N_2 and 21% vol. O_2) obtained with the RFM and validated against reference data from NIST REFPROP for a predefined air mixture (78.12% vol. N_2, 20.96% vol. O_2, and 0.92% vol. Ar). Good agreement is observed for all three properties. However, some deviations in λ occur at temperatures higher than 600 K, while c_p shows a continuous offset across the temperature range. These differences might be explained by the different modeling used in REFPROP and the inclusion of Argon in the predefined mixture.

A combination between the pT flash solver used in Section IV.B to calculate the distillation curves of the fuel surrogates and the representation of saturated bubble and dew lines can be used to illustrate the VLE between the fuel mixture and air. Although the interface-resolving methodology presented in Section III for the droplet evaporation study differs in nature, the same transcritical features are captured. For this purpose, a mixture between C-1 and air has been defined with a total mass concentration of 1.4548% iC10, 70.8023% iC12, 6.3043% iC13, 15.5183% iC16, 2.9098% iC20, 0.7015% O_2, and 2.3090% N_2. These values have been obtained by assuming an idealized condition at atmospheric pressure (i.e., 1 bar) and room temperature (i.e., 298 K) where all fuel species remain in the liquid

phase and all air species remain in the gas phase. Then, the amount of air is controlled by assuming it occupies twenty times the volume of liquid fuel.

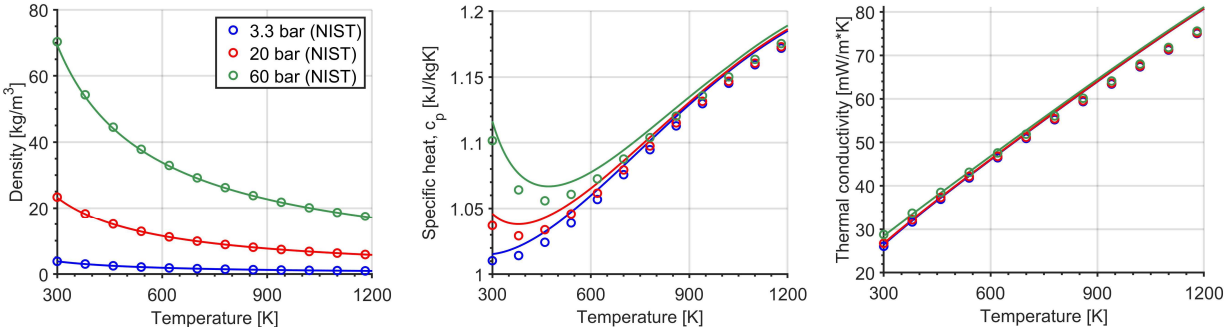

(a) density (b) isobaric specific heat (c) thermal conductivity

Fig. 5 Properties of air (79% vol. N_2 and 21% vol. O_2) at different target conditions. Results for air are compared against reference data from NIST REFPROP. (a) density; (b) isobaric specific heat; (c) thermal conductivity.

Note that the uncertainties in the proposed RFM increase when the fluid mixtures include components with substantially different properties [8]. As discussed in Section III.B, k_{ij} are neglected. However, the major trends are captured and relevant conclusions on the non-ideal fluid behavior at these conditions can be extracted. Figure 6a shows the distillation curves at 3.3 bar, 20 bar, and 60 bar of the considered C-1 + air mixture. Note that a two-phase region exists above the critical pressure of C-1. Moreover, the inclusion of air components in the mixture also causes deviations in the distillation curve compared to the pure fuel (i.e., see 3.3 bar case). At low temperatures, the vapor is mainly composed of N_2 and O_2 and, as temperature increases, the fuel species start vaporizing earlier. Nonetheless, the vaporization trends become similar toward the end of the boiling range. This is especially true in low pressure conditions where the dissolution of ambient gas in the liquid phase is negligible. Also, note the incomplete distillation path at 60 bar. That is, vapor initially forms but the mixture returns to a liquid state as temperature increases. As shown in Fig. 6b, retrograde phenomena may occur for these complex multi-component mixtures and a maximum pressure of two-phase coexistence (i.e., cricondenbar) exists above the critical pressure of the mixture. Thus, any two-phase path (L+V) above the critical pressure results in the mixture returning to a liquid state (L). Below p_c, the liquid phase reaches a complete vaporization as temperature increases (V). Moreover, Fig. 6c visualizes the enhanced dissolution of N_2 and O_2 into the liquid with increasing pressure. The impact of the ambient gas dissolution and the preferential evaporation of the fuel species on the liquid mixture properties have been previously discussed [8] and is further highlighted in the present work (see Section IV.E). Note that the discussed figures will be different depending on the total amount of air in the homogeneous mixture (i.e., higher amounts of air will result in greater transcritical effects).

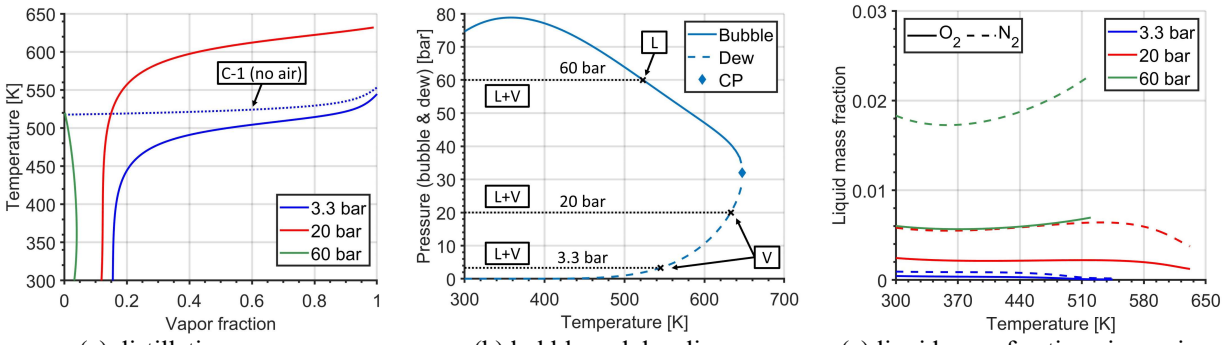

(a) distillation curves (b) bubble and dew lines (c) liquid mass fraction air species

Fig. 6 Vapor-liquid equilibrium characteristics of a homogeneous mixture of C-1 and air (79% vol. N_2 and 21% vol. O_2) at different target conditions. (a) distillation curves; (b) bubble and dew lines; (c) liquid mass fraction of dissolved air species.

D. Droplet Model Validation

The droplet model presented in Section III is validated against experimental data from Nomura et al. [50] and the computational results from Zhu and Aggarwal [18] and Zhang [51]. A pure n-heptane droplet with d0 = 0.5 mm and $T_{drop} = 300$ K is suddenly immersed in a quiescent gaseous nitrogen environment initially at a constant temperature $T_{g,\infty}$. For this validation, non-zero k_{ij} values are used in the mixing rules from Eq. (8), as suggested in [18]. Three ambient conditions are considered representative of the pressure and temperature ranges shown in Table 1: (i) $p = 5$ bar and $T_{g,\infty} = 655$ K; (ii) $p = 20$ bar and $T_{g,\infty} = 746$ K; and (iii) $p = 50$ bar and $T_{g,\infty} = 453$ K. Additionally, a grid convergence study is performed ranging from an initial resolution of 25 cells/diameter (i.e., c/d0) to 100 c/d0. The droplet lifetime and the relaxation to the d^2 law are chosen as validation parameters (see Fig. 7). Grid independence is achieved quickly, and minor differences are observed between the three tested resolutions. This conclusion applies to both the evolution of the droplet radius and the interface state (e.g., equilibrium temperature, mass flux). Due to the computational cost, the 5 and 20 bar cases with 100 c/d0 do not run until complete vaporization but still show good convergence trends. For the fuel surrogate droplets discussed in Section IV.E, a resolution of 50 c/d0 is chosen to balance numerical accuracy with the greater computational cost associated with multi-component mixtures.

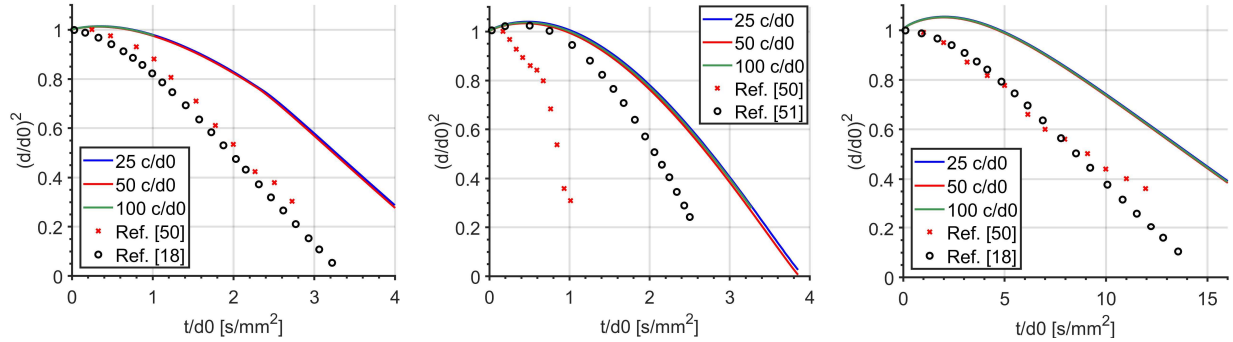

(a) $p = 5$ bar & $T_{g,\infty} = 655$ K (b) $p = 20$ bar & $T_{g,\infty} = 746$ K (c) $p = 50$ bar & $T_{g,\infty} = 453$ K

Fig. 7 Validation of droplet lifetimes of a n-heptane droplet immersed in a quiescent nitrogen environment. (a) $p = 5$ bar & $T_{g,\infty} = 655$ K; (b) $p = 20$ bar & $T_{g,\infty} = 746$ K; (c) $p = 50$ bar & $T_{g,\infty} = 453$ K.

Note that modeling uncertainties greatly affect the transient process depending on the assumptions in the governing equations and the chosen thermophysical models. For example, volumetric expansion in the liquid is neglected in [18]. Thus, the initial transient where droplet heating results in thermal expansion is not represented. In contrast, this phenomenon is captured by the model proposed in this work and by [51]. Moreover, the volumetric expansion induced by the dissolution of the lighter air components (i.e., nitrogen in this case) at very high pressures is included. The experimental data in [50] shows almost no volume expansion of the droplet as a consequence of the experimental setup itself inducing a rapid droplet heat-up before measurements are taken, as explained in [51]. The impact of using a different equation of state on the prediction of droplet lifetimes is shown in [18]. The differences come mostly from the evaluation of fluid and transport properties rather than the VLE solution at the interface. In other words, the quiescent droplet evaporation case is highly sensitive to the heating rate of the droplet, mainly given by the predicted thermal conductivity and specific heat. Regardless of these observations, the proposed droplet model coupled to the thermophysical model based on the VT-SRK EoS reproduces the relevant physics. The evaporation rates and droplet lifetimes are well within the expected values, and the quasi-linear evolution of $(d/d0)^2$, approximating the d^2 law, agrees well with experimental data, especially at 5 bar and 50 bar.

E. Droplet Evaporation of Category C Fuel Surrogates

The droplet characteristics of the four Category C fuel surrogates introduced in Section IV.A are analyzed at the target conditions discussed in Section III.D for the quiescent environment scenario. Initially, the liquid mixture only contains fuel species with the compositions detailed in Fig. 1, while the gaseous phase is a mixture of nitrogen and oxygen characteristic of the ORZ or the CRZ (see Table 1). The droplet temperature is initially uniform. However, a temperature distribution is imposed in the gas phase near the interface to alleviate the initial sharp condition. Otherwise, the multi-component VLE solver might struggle to converge during the first few iterations. Note that this initialization differs from that of Section IV.D with a binary system that easily converges. Nonetheless, a thin mixing layer may already form around the droplets during the atomization process. As an example, Fig. 8 shows the initial temperature profiles for cruise conditions in the ORZ and CRZ. A hyperbolic tangent profile is imposed following

$T = (T_{g,\infty} - T_{drop})\tanh[(800/T_{g,\infty})(r - r_{drop}) \times 10^6] + T_{drop}$ for $r \geq r_{drop}$. Note that the initial thermal layer only extends a few microns (e.g., 2.4 μm for ORZ and 3.7 μm for CRZ in Fig. 8).

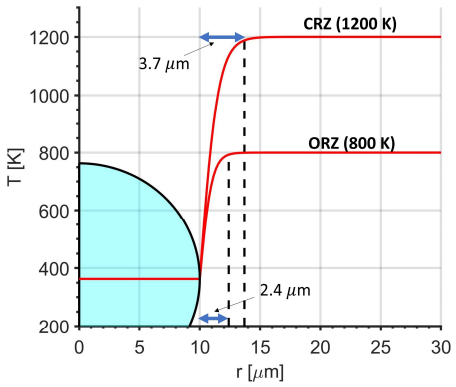

Fig. 8 Initial temperature distribution for cruise operating conditions defined in Table 1. Similar distributions follow for LBO and take-off.

A comparison of droplet lifetimes among the different fuel surrogates and target conditions is provided in Fig. 9 using real time scales. Note that the LBO cases in the ORZ for C-1 and C-2 are not complete to full evaporation of the droplet mainly due to computational costs. Nonetheless, relevant conclusions can be extracted. The droplet lifetimes are on the order of a few milliseconds for both cruise conditions and LBO in the CRZ, while droplets in the ORZ at LBO conditions require longer times to fully vaporize (i.e., an order of magnitude greater) due to the lower ambient temperature. Note that for C-1, the evaporation rates drop significantly after some time. This illustrates the importance of properly characterizing the two-phase behavior of the fuel at LBO conditions due to the longer timescales associated with the evaporation process, which affect the fuel vapor spatial distribution, the subsequent combustion downstream and the engine operability. In contrast, the time scales for take-off conditions are much shorter (10^{-2}-10^{-1} ms) mainly due to the smaller initial diameter. For LBO and cruise conditions, a two-phase interface is sustained until the droplets fully vaporize. However, at take-off conditions the droplets may experience a transition to a supercritical state during the evaporation process where the two-phase interface disappears and cannot be captured with the proposed model. Although not done in this work, it would be possible to continue the simulations by eliminating the interface and solving the single-phase governing equations [18,19] while at the same time keeping track of the possibility of phase separation occurring again.

The details of the droplet evaporation dynamics can be better understood by looking at interface composition and temperature plots to analyze preferential evaporation effects and phase transitions. Fig. 10 shows the interfacial temperature of all the droplets, while Fig. 11 only shows the liquid and vapor interface compositions of select cases of C-1 for brevity. Since the initial droplet diameter and temperature distributions are identical for each operating point, fuel effects are observed. In general, C-1 and C-1ez droplets behave very similarly and differences are only evident toward the end of the droplet's life. That is, when the droplet temperature has increased enough for the preferential evaporation effects to be more noticeable between both surrogates. For example, the existence of iC20 with lower volatility in C-1 enhances the bimodal distillation behavior of the surrogate (see Fig. 3a) and extends the droplet lifetime while allowing higher interface temperatures compared to C-1ez. This is observed in, e.g., Fig. 11e when most of the liquid phase is iC20 toward the end of the droplet's life. As the C-1 droplets are depleted of iC12 and iC16 in favor of iC20, clear changes in the slope of $(d/d0)^2$ are observed between C-1 and C-1ez, meaning evaporation rates are changing substantially (e.g., around 1.4 ms in the ORZ or 0.6 ms in the CRZ for cruise conditions). For LBO conditions in the ORZ, this effect is exaggerated and the droplet regression rate for C-1 seems to plateau as not enough thermal energy is available to vaporize iC20 efficiently. Additionally, preferential evaporation effects, visualized through the changing slope in $(d/d0)^2$, are highly dependent on the ambient conditions. The evaporation rates of C-1ez droplets are affected by preferential evaporation at LBO conditions, but seemingly disappear at higher pressures (cruise or take-off). In contrast, C-1 still displays some preferential evaporation effects on $(d/d0)^2$ at cruise conditions, but not at take-off. These observations indicate that, as pressure increases, the bimodal nature of the distillation curves of C-1ez/C-1 at low pressure is lost and a more uniform evaporation process occurs. A similar behavior was observed in [8].

The other fuel surrogates also present distinct features. Note that C-2 does not show a clear change in the slope of $(d/d0)^2$ for any configuration despite having a bimodal distillation curve since bM3 evaporates relatively quickly;

thus, iC14 dominates most of the droplet evaporation dynamics. Moreover, C-2 droplets consistently need longer times to fully vaporize compared to C-1/C-1ez and C-5 due to being mostly iC14 (i.e., low volatility). One exception might occur at LBO conditions in the ORZ where C-1 might take substantially longer times. Regardless of the slower evaporation rates across the operating environment, the interface temperatures are in line with those of C-1 and C-1ez. Then, C-5 droplets reach the lowest temperatures while typically evaporating faster than the other fuel surrogates as they are composed of higher volatility components. The only exception is observed for cruise conditions with droplet lifetimes being similar to those of C-1ez. Changes in the slope of $(d/d0)^2$ are also negligible for C-5 due to the relatively flat boiling of the fuel. Thus, having evaporation features resembling pure hydrocarbon droplets.

The composition plots in Fig. 11 for C-1 reveal the expected preferential evaporation trends and the increasing concentration of fuel vapor as the droplets evaporate. The mass fractions of N_2 and O_2 decrease rapidly in favor of iC12 vapor, which is the first major component of C-1 to evaporate, later followed by iC16 and iC20. Aligned with this, the composition on the liquid side shows the mass fraction of iC12 dropping as the concentrations of iC16 and iC20, the least volatile components, increase. An important characteristic of high-pressure interface thermodynamics is the increased dissolution of ambient gas into the liquid phase, which has been previously discussed in Section IV.C. At the low pressures associated with LBO, the concentration of N_2 and O_2 in the liquid is negligible (see Fig. 11d), but it increases with increasing pressure (see Fig. 11f). Similar trends are shown in Fig. 6c obtained with the pT flash solver.

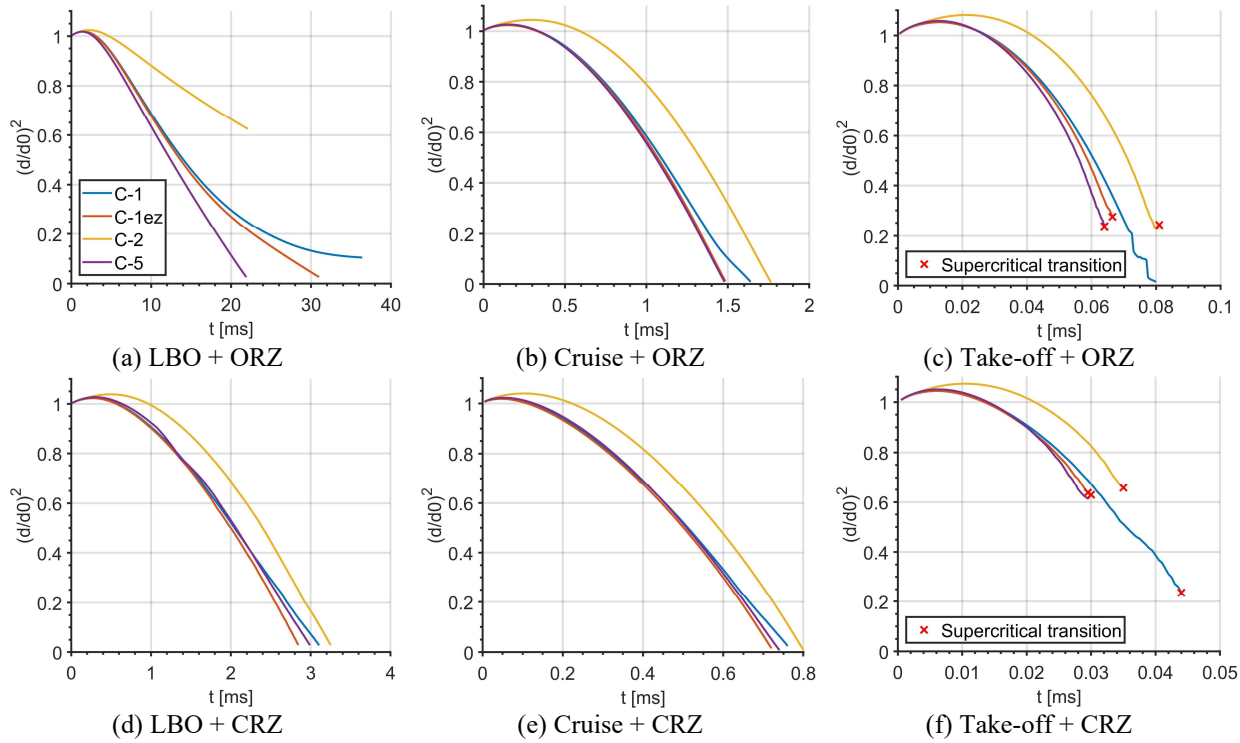

Fig. 9 Droplet lifetimes of Category C fuel surrogates droplets immersed in a quiescent air environment at various operating conditions described in Table 1. (a) LBO + ORZ; (b) Cruise + ORZ; (c) Take-off + ORZ; (d) LBO + CRZ; (e) Cruise + CRZ; (f) Take-off + CRZ.

The transition to a supercritical state of the droplet's surface is highlighted in the respective take-off plots. It occurs half-way through the evaporation process, signaling that transcritical effects are important at 60 bar. That is, regions of two-phase dynamics can be expected. In the ORZ, droplets of C-1ez, C-2 and C-5 almost completely vaporize before reaching the critical state. A two-phase interface exists for C-1 until the end of the droplet's lifetime due to the presence of iC20 in the mixture, which has a much higher critical temperature than the components present in the other fuel surrogates. However, some oscillations are observed toward the end of the vaporization process (discussed in the following paragraph). In contrast, a critical state is reached for all fuel surrogates in the CRZ, with C-1 sustaining a two-phase interface for longer. Here, the critical state is identified when the compositions of the liquid and vapor sides of the interface become identical (see Figs. 11c and 11f). Note that for C-1ez, C-2 and C-5, the critical temperatures at the droplet surface when the supercritical transition occurs are similar to those reported for the critical

point of the pure fuel surrogates (i.e., with no air species) in Section IV.B. Nonetheless, the C-1 droplet in the CRZ is able to reach much higher temperatures before transitioning to a supercritical state. The behavior of C-1 is not unexpected given the complexities of the multi-component VLE with a surrounding ambient gas and the corresponding changes in mixture critical points. Nonetheless, it seems to be possible to use the fuel critical point to estimate phase transitions of some SAF surrogates, even in complex scenarios.

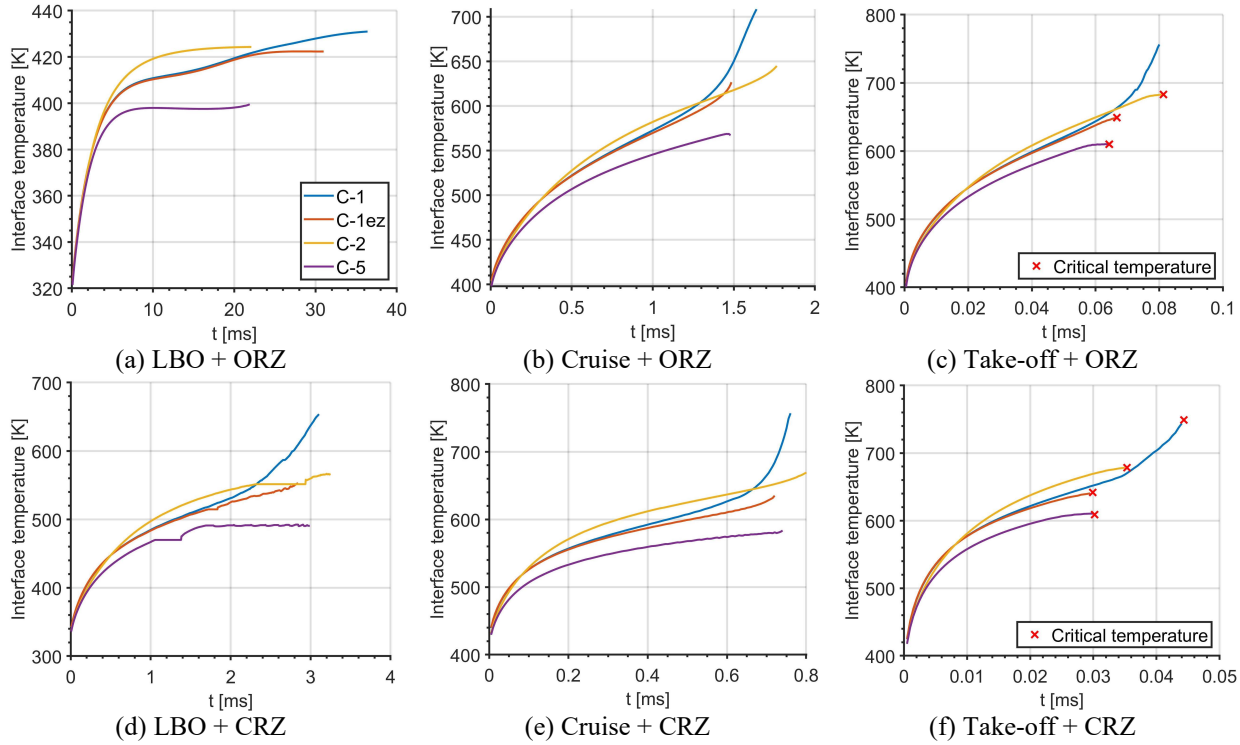

Fig. 10 Interface temperature of Category C fuel surrogates droplets immersed in a quiescent air environment at various operating conditions described in Table 1. (a) LBO + ORZ; (b) Cruise + ORZ; (c) Take-off + ORZ; (d) LBO + CRZ; (e) Cruise + CRZ; (f) Take-off + CRZ.

Although in general not affecting the stability of the numerical solution, it is worth noting that Figs. 9 to 11 show some oscillations in the interface equilibrium solution and a smooth curve is not always observed, especially for LBO conditions in the CRZ and take-off conditions as the droplet's surface approaches a critical state. These originate from a combination of the numerical approach dealing with the moving interface (see Section III.C) and the sensitivities of the VLE solver, i.e., due to the large variations in fugacity and composition near the mixture critical point at take-off (high pressures), or due to the negligible dissolution of air components into the liquid phase at LBO (low pressures). Some possible solutions to this problem are: (i) to investigate the robustness and tolerance of the numerical solver used to solve the system of equations defining the VLE to find best practices; (ii) for low pressures, using an ideal multi-component VLE approach neglecting the dissolution of air components has been shown to be reasonably accurate for Category C fuel surrogates [8]; and (iii) mesh refinement might control better the oscillations as the interface crosses the nodes. Given the scope of this paper, this is left for future work.

The discussion provided in the previous paragraphs is solely based on the observed droplet lifetimes and the composition and preferential evaporation characteristics of each surrogate mixture. Although fuel properties are shown to be similar at ambient pressures and relatively low temperatures (e.g., Fig. 2), a deeper analysis may provide more insights into the transient evaporation process, droplet lifetimes, and the role of each physical process (e.g., mass diffusion). For this purpose, the radial distributions of some variables for the C-1 case at cruise conditions in the CRZ are discussed below.

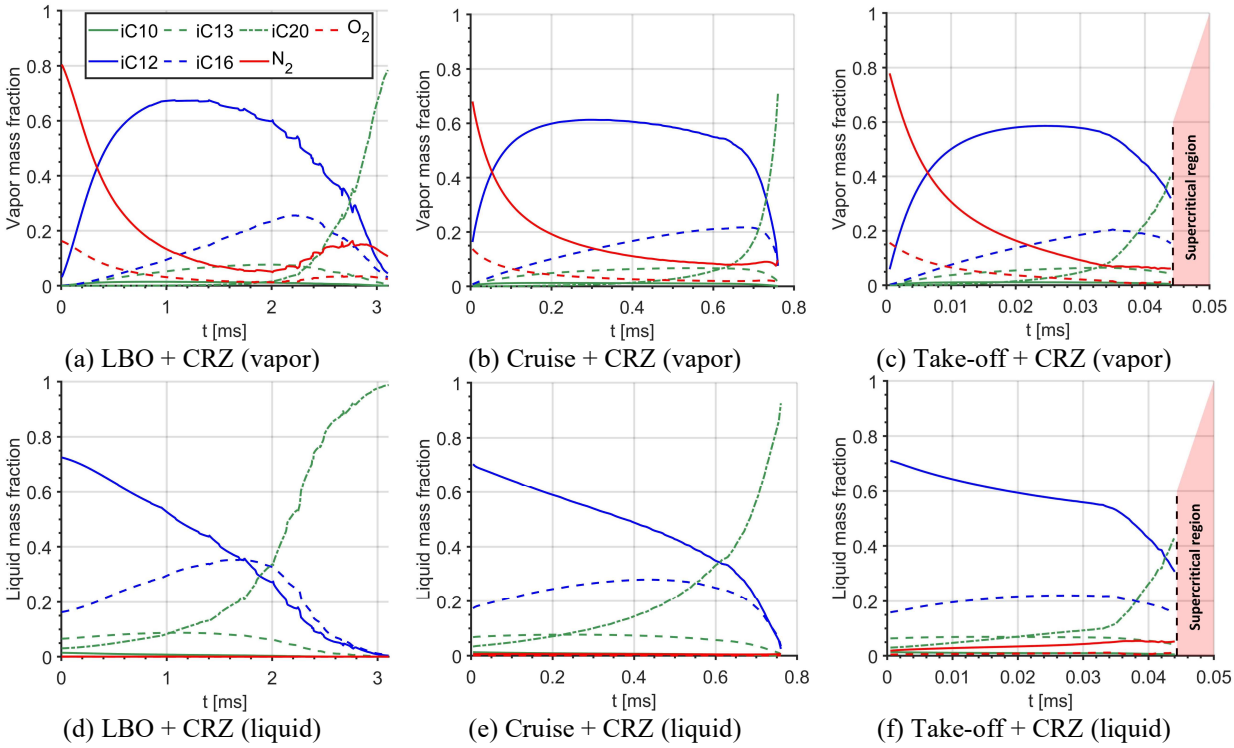

(a) LBO + CRZ (vapor) (b) Cruise + CRZ (vapor) (c) Take-off + CRZ (vapor)

(d) LBO + CRZ (liquid) (e) Cruise + CRZ (liquid) (f) Take-off + CRZ (liquid)

Fig. 11 Vapor and liquid interface mass fractions of C-1 droplets immersed in a quiescent air environment at various operating conditions described in Table 1. (a) LBO + CRZ (vapor); (b) Cruise + CRZ (vapor); (c) Take-off + CRZ (vapor); (d) LBO + CRZ (liquid); (e) Cruise + CRZ (liquid); (f) Take-off + CRZ (liquid).

Fig. 12 shows snapshots of the temperature field inside and in the vicinity of the droplet surface, as well as the interface location and temperature. The figure highlights the cooling of the vapor and heating of the droplet over time. Initially, large temperature gradients occur inside the droplet, but toward the end of the evaporation process the droplet temperature becomes more uniform. Similarly, Fig. 13 presents the mass fraction distributions of iC12, iC16 and iC20, and Fig. 14 shows the profiles of density, thermal conductivity and isobaric specific heat. The visualization of these variables further improves the understanding of preferential evaporation in the multi-component droplet. As the various hydrocarbons vaporize, the fuel vapor always diffuses away from the interface. This information is extracted from the mass fraction gradients and no uphill diffusion seems to occur (ie., diffusion opposing the natural direction given by the composition gradient). However, different dynamics are shown in the liquid phase. The droplet is constantly being depleted of iC12, with this species always diffusing toward the droplet's surface (see Fig. 13a). Since iC12 vaporizes more easily, the concentrations of iC16 and iC20 increase at the interface (like in Fig. 11) and these species diffuse into the droplet. Close to the complete vaporization of the droplet, a reversal occurs for iC16. At 0.70 ms (see Fig 13b), the droplet's temperature has increased substantially and iC16 vaporizes more easily; thus, its concentration at the interface drops and iC16 diffuses from inside the droplet toward its surface. During this process, the concentration of iC20 inside the droplet rapidly increases (see Fig. 13c).

Fig. 14 reveals that the droplet undergoes sharp variations in fluid properties as it vaporizes. The behavior of vapor properties is as expected, so it is not discussed in detail here. At 0.05 ms, the droplet core remains at the initial low temperature while higher temperatures are observed near the interface (Fig. 12), and the droplet composition is still fairly uniform. Thus, the expected trends where ρ and λ decrease away from the droplet center, but c_p increases, are observed. Similar trends are shown for ρ and c_p at 0.25 ms and 0.50 ms despite the composition varying more significantly across the droplet, suggesting these properties are mostly responding to the temperature variations. However, the distribution of λ is affected by preferential evaporation earlier and shows a trend reversal at 0.50 ms, being larger in regions with higher concentrations of the heavier hydrocarbons. Once the droplet temperature becomes more uniform at 0.70 ms, the effects of preferential evaporation in the fluid properties are enhanced. The density and thermal conductivity are substantially lower in the center of the droplet compared to near its surface. In contrast, the specific heat is larger. Such differences occur since the liquid mixture still has 60% in mass of iC12 in the droplet's

center and is subjected to very high temperatures close to the critical temperature of iC12 (i.e., 628.62 K). In other words, the fluid properties in this region display transcritical features and are strongly affected by the non-linearities in the vicinity of critical points (see Fig. 4 for C-1 at 20 bar). The thermal diffusivity, $\alpha = \lambda/(\rho c_p)$, inside the droplet is plotted in Fig. 15 as a measure of thermal diffusion into the droplet. Note that α stabilizes over time, leading to the first nearly linear slope of $(d/d0)^2$ in Fig. 9e. However, α varies sharply again at 0.70 ms, with a substantial decrease toward the center of the droplet as λ drops and c_p rises. This translates into a reduced thermal diffusion into the droplet, increased surface temperature (see Fig. 10e) and a change in evaporation rate and slope of $(d/d0)^2$.

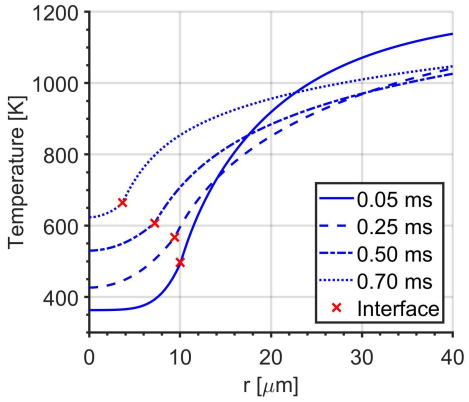

Fig. 12 Temperature across a C-1 droplet at cruise conditions in the CRZ.

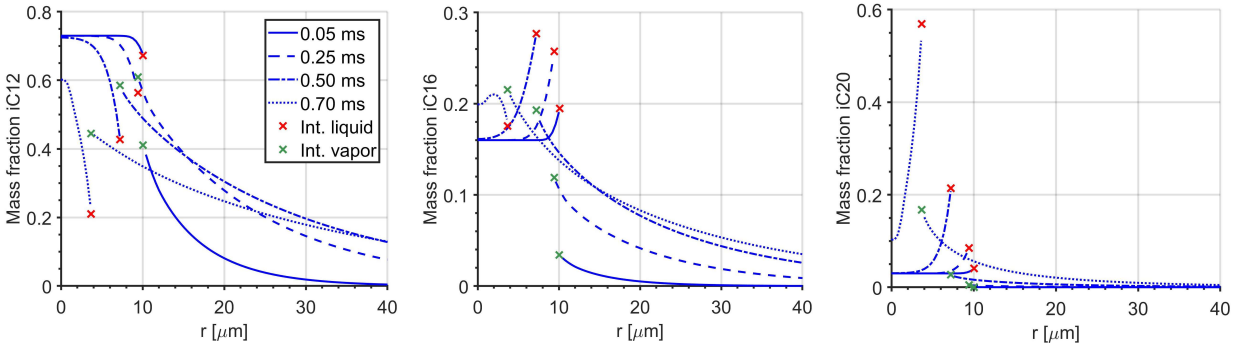

(a) iso-dodecane (b) iso-hexadecane (c) iso-icosane

Fig. 13 Mass fraction across a C-1 droplet at cruise conditions in the CRZ. (a) iso-dodecane; (b) iso-hexadecane; (c) iso-icosane.

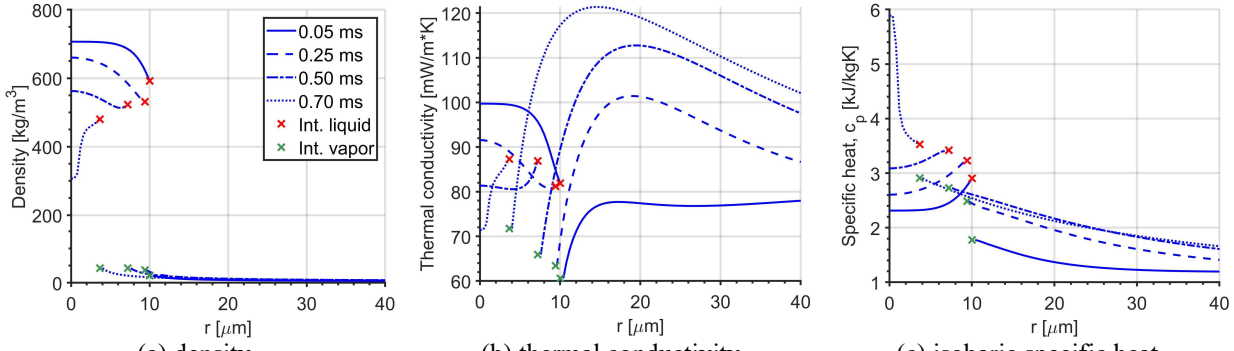

(a) density (b) thermal conductivity (c) isobaric specific heat

Fig. 14 Fluid properties across a C-1 droplet at cruise conditions in the CRZ. (a) density; (b) thermal conductivity; (c) isobaric specific heat.

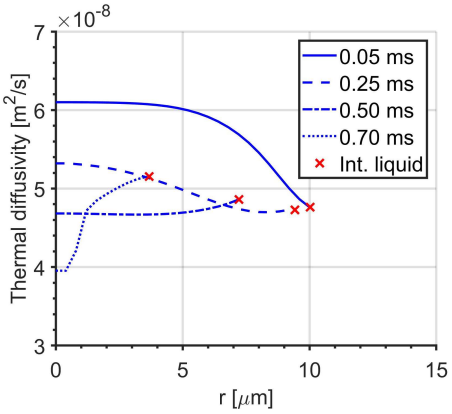

Fig. 15 Thermal diffusivity across a C-1 droplet at cruise conditions in the CRZ.

V. Conclusions

This paper presented a droplet model coupled with real-fluid thermodynamics to study the evaporation of droplets of Category C fuel surrogates (i.e., SAF candidates) in a quiescent air environment under various jet engine operating conditions. This study is an important first step to explore multi-component droplet evaporation dynamics of realistic SAF surrogates and has shown that candidate biofuels present distinct evaporation features that affect the droplet lifetimes or the transition to a supercritical state at high pressures and temperatures. For example, droplets submerged in high temperature gases (900 K or more) evaporate completely inside the two-phase envelope at LBO and cruise conditions. However, this is not the case at take-off conditions where most of the tested fuels transition to a supercritical state. Preferential evaporation is particularly important for C-1 as the presence of 3% in mass of iC20, a heavy hydrocarbon with very low volatility, results in extended droplet lifetimes and regions of two-phase coexistence when compared to C-5 or C-1ez, a binary surrogate of POSF# 13718 usually assumed in the literature. Moreover, the multi-component nature of the fuel mixtures may cause considerable variations of fluid properties inside the droplet, which may modify the evaporation rates over time and define the fuel-oxidizer mixing and combustion processes.

Future work should extend the study to droplets submerged in convective flows (e.g., similar to [51]) to consider more realistic scenarios with the goal of developing comprehensive evaporation models. That is, taking into account not only preferential evaporation effects, but also convective heat transfer and flow recirculation inside the droplet. Moreover, these studies might offer insights into the variable surface tension coefficient that emerges during the heating and preferential evaporation of the droplets and be used to inform breakup models.

Acknowledgments

The submitted manuscript has been created by UChicago Argonne, LLC, Operator of Argonne National Laboratory (“Argonne”). Argonne, a U.S. Department of Energy Office of Science laboratory, is operated under Contract No. DE-AC02-06CH11357. The U.S. Government retains for itself, and others acting on its behalf, a paid-up nonexclusive, irrevocable worldwide license in said article to reproduce, prepare derivative works, distribute copies to the public, and perform publicly and display publicly, by or on behalf of the Government. The Department of Energy will provide public access to these results of federally sponsored research in accordance with the DOE Public Access Plan. http://energy.gov/downloads/doe-public-access-plan

This work has been funded by the DOE Office of Energy Efficiency and Renewable Energy. The authors wish to thank Kevin Stork and Gurpreet Singh at the DOE Vehicle Technologies Office for their support.

The authors acknowledge the use of computational resources of DelftBlue supercomputer, provided by Delft High Performance Computing Centre (https://www.tudelft.nl/dhpc).

References

[1] Colket, M., Heyne, J., Rumizen, M., Gupta, M., Edwards, T., Roquemore, W.M., Andac, G., Boehm, R., Lovett, J., Williams, R., Condevaux, J., Turner, D., Rizk, N., Tishkoff, J., Li, C., Moder, J., Friend, D., Sankaran, V., “Overview of the National Jet Fuels Combustion Program,” *AIAA Journal*, Vol. 55, No. 4, 2017, pp. 1087-1104. https://doi.org/10.2514/1.J055361, URL https://doi.org/10.2514/1.J055361

[2] Dasgupta, D., Sibendu, S., Wood, E., Lee, T., Mayhew, E., Temme, J., Kweon, C.-B., "Computational Fluid Dynamics Modeling of Fuel Properties Impact on Lean Blowout in the ARC-M1 Combustor," *Proceedings of the ASME Turbo Expo 2022: Turbomachinery Technical Conference and Expostition. Volume 3A: Combustion, Fuels, and Emissions*, Rotterdam, Netherlands, 2022, V03AT04A010. https://doi.org/10.1115/GT2022-79347, URL https://doi.org/10.1115/GT2022-79347

[3] Edwards, T., "Reference Jet Fuels for Combustion Testing," *55th AIAA Aerospace Science Meeting*, American Institute of Aeronautics and Astronautics, Grapevine, TX, 2017. https://doi.org/10.2514/6.2017-0146, URL https://arc.aiaa.org/doi/abs/10.2514/6.2017-0146

[4] Boehm, R.C., Hauck, F., Yang, Z., Wanstall, C.T., Heyne, J.S., "Error Quantification of the Arrhenius Blending Rule for Viscosity of Hydrocarbon Mixtures," *Frontiers in Energy Research*, Vol. 10, 2022, pp. 1074699. https://doi.org/10.3389/fenrg.2022.1074699, URL https://www.frontiersin.org/articles/10.3389/fenrg.2022.1074699

[5] Colket, M., Edwards, T., Williams, S., Cernansky, N.P., Miller, D.L., Egolfopoulos, F., Lindstedt, P., Seshadri, K., Dryer, F.L., Law, C.K., Friend, D., Lenhert, D.B., Pitsch, H., Sarofim, A., Smooke, M., Tsang, W., "Development of an Experimental Database and Kinetic Models for Surrogate Jet Fuels," *45th AIAA Aerospace Science Meeting*, American Institute of Aeronautics and Astronautics, Reno, NV, 2007. https://doi.org/10.2514/6.2007-770, URL https://arc.aiaa.org/doi/abs/10.2514/6.2007-770

[6] Galbiati, C., Tonini, S., Conti, P., Cossali, G.E., "Numerical Simulations of Internal Flow in an Aircraft Engine Pressure Swirl Atomizer," *Journal of Propulsion and Power*, Vol. 32, No. 6, 2016, pp. 1433-1441. https://doi.org/10.2514/1.B35944, URL https://arc.aiaa.org/doi/full/10.2514/1.B35944

[7] Poblador-Ibanez, J., Nocivelli, L., "Modeling of Sustainable Aviation Fuels with Real-Fluid Equations of State," *ILASS-Americas 33rd Annual Conference on Liquid Atomization and Spray Systems*, Albuquerque, NM, 2023.

[8] Poblador-Ibanez, J., Nocivelli, L., "Toward a Real-Fluid Modeling Framework for Sustainable Aviation Fuels," 2023. In press at *Fuel Communications. Special Issue: Carbon Neutral Synthetic Fuels for Mobility and Transport.* https://doi.org/10.1016/j.jfueco.2023.100100, URL https://www.sciencedirect.com/science/article/pii/S266605202300016X

[9] Wang, X., Wang, Y., Yang, V., "Three-Dimensional Flow Dynamics and Mixing in a Gas-Centered Liquid-Swirl Coaxial Injector at Supercritical Pressure," *Physics of Fluids*, Vol. 31, No. 6, 2019, pp. 065109. https://doi.org/10.1063/1.5097163, URL https://pubs.aip.org/aip/pof/article/31/6/065109/1068599/

[10] Sciacovelli, L., Bellan, J., "The Influence of the Chemical Composition Representation According to the Number of Species During Mixing in High-Pressure Turbulent Flows," *Journal of Fluid Mechanics*, Vol. 863, 2019, pp. 293-340. https://doi.org/10.1017/jfm.2018.992, URL https://doi.org/10.1017/jfm.2018.992

[11] Fathi, M., Hickel, S., Roekaerts, D., "Large Eddy Simulations of Reacting and Non-Reacting Transcritical Fuel Sprays Using Multiphase Thermodynamics," *Physics of Fluids*, Vol. 34, No. 8, 2022, pp. 085131. https://doi.org/10.1063/5.0099154, URL https://pubs.aip.org/aip/pof/article/34/8/085131/2847551/

[12] Gaballa, H., Habchi, C., de Hemptinne, J.-C., "Modeling and LES of High-Pressure Liquid Injection Under Evaporating and Non-Evaporating Conditions by a Real Fluid Model and Surface Density Approach," *International Journal of Multiphase Flow*, Vol. 160, 2023, pp. 104372. https://doi.org/10.1016/j.ijmultiphaseflow.2022.104372, URL https://www.sciencedirect.com/science/article/pii/S0301932222003317

[13] Tamim, J., Hallett, W.L.H., "A Continuous Thermodynamics Model for Multicomponent Droplet Vaporization," *Chemical Engineering Science*, Vol. 50, No. 18, 1995, pp. 2933-2942. https://doi.org/10.1016/0009-2509(95)00131-N, URL https://www.sciencedirect.com/science/article/pii/000925099500131N

[14] Le Clercq, P.C., Bellan, J., "Direct Numerical Simulation of Gaseous Mixing Layers Laden with Multicomponent-Liquid Drops: Liquid-Specific Effects," *Journal of Fluid Mechanics*, Vol. 533, 2005, pp. 57-94. https://doi.org/10.1017/S0022112005003940, URL https://doi.org/10.1017/S0022112005003940

[15] Le Clercq, P.C., Doué, N., Rachner, M., Aigner, M., "Validation of a Multicomponent-Fuel Model for Spray Computations," *47th AIAA Aerospace Science Meeting*, American Institute of Aeronautics and Astronautics, Orlando, FL, 2009. https://doi.org/10.2514/6.2009-1188, URL https://arc.aiaa.org/doi/abs/10.2514/6.2009-1188

[16] Cooney, A.Y., Singer, S.L., "Modeling of Multicomponent Fuel Droplet Vaporization with Finite Liquid Diffusivity Using Coupled Algebraic-DQMoM with Delumping," *Fuel*, Vol. 212, 2018, pp. 554-565. https://doi.org/10.1016/j.fuel.2017.10.056, URL https://www.sciencedirect.com/science/article/pii/S0016236117312978

[17] Burger, M., Schmehl, R., Prommersberger, K., Schäfer, O., Koch, R., Wittig, S., "Droplet Evaporation Modeling by the Distillation Curve Model: Accounting for Kerosne Fuel and Elevated Pressures," *International Journal of Heat and Mass Transfer*, Vol. 46, No. 23, 2003, pp. 4403-4412. https://doi.org/10.1016/S0017-9310(03)00286-2, URL https://www.sciencedirect.com/science/article/pii/S0017931003002862

[18] Zhu, G.S., Aggarwal, S.K., "Transient Supercritical Droplet Evaporation with Emphasis on the Effects of Equation of State," *International Journal of Heat and Mass Transfer*, Vol. 43, No. 7, 2000, pp. 1157-1171. https://doi.org/10.1016/S0017-9310(99)00197-0, URL https://www.sciencedirect.com/science/article/pii/S0017931099001970

[19] He, P., Ghoniem, A.F., "A Sharp Interface Method for Coupling Multiphase Flow, Heat Transfer and Multicomponent Mass Transfer with Interphase Diffusion," *Journal of Computational Physics*, Vol. 332, 2017, pp. 316-332. https://doi.org/10.1016/j.jcp.2016.12.002, URL https://www.sciencedirect.com/science/article/pii/S002199911630643X

[20] Delplanque, J.-P., Sirignano, W.A., "Numerical Study of the Transient Vaporization of an Oxygen Droplet at Sub- and Super-critical Conditions," *International Journal of Heat and Mass Transfer*, Vol. 36, No. 2, 1993, pp. 303-314. https://doi.org/10.1016/0017-9310(93)80006-G, URL https://www.sciencedirect.com/science/article/pii/001793109380006G

[21] Poblador-Ibanez, J., Sirignano, W.A., "Transient Behavior Near Liquid-Gas Interface at Supercritical Pressure," *International Journal of Heat and Mass Trasnfer*, Vol. 126, 2018, pp. 457-473. https://doi.org/10.1016/j.ijheatmasstransfer.2018.05.066, URL https://www.sciencedirect.com/science/article/pii/S0017931018309505

[22] Poblador-Ibanez, J., Sirignano, W.A., "A Volume-of-Fluid Method for Variable-Density, Two-Phase Flows at Supercritical Pressure," *Physics of Fluids*, Vol. 34, No. 5, 2022, pp. 053321. https://doi.org/10.1063/5.0086153, URL https://pubs.aip.org/aip/pof/article/34/5/053321/2847079/

[23] Leahy-Dios, A., Firoozabadi, A., "Unified Model for Nonideal Multicomponent Molecular Diffusion Coefficients," *AIChE Journal*, Vol. 53, No. 11, 2007, pp. 2932-2939. https://doi.org/10.1002/aic.11279, URL https://aiche.onlinelibrary.wiley.com/doi/full/10.1002/aic.11279

[24] Liu, X., Martín-Calvo, A., McGarrity, E., Schnell, S.K., Calero, S., Simon, J.-M., Bedeaux, D., Kjelstrup, S., Bardow, A., Vlugt, T.J.H., "Fick Diffusion Coefficients in Ternary Liquid Systems from Equilibrium Molecular Dynamics Simulations," *Industry & Engineering Chemistry Research*, Vol. 51, No. 30, 2012, pp. 10247-10258. https://doi.org/10.1021/ie301009v, URL https://pubs.acs.org/doi/10.1021/ie301009v

[25] Jofre, L., Urzay, J., "Transcritical Diffuse-Interface Hydrodynamics of Propellants in High-Pressure Combustors of Chemical Propulsion Systems," *Progress in Energy and Combustion Science*, Vol. 82, 2021, pp. 100877. https://doi.org/10.1016/j.pecs.2020.100877, URL https://www.sciencedirect.com/science/article/pii/S0360128520300873

[26] Poling, B.E., Prausnitz, J.M., O'Connell, J.P., *The Properties of Gases and Liquids*, 5th ed., McGraw-Hill Education, 2001.

[27] Lin, H., Duan, Y.-Y., Zhang, T., Huang, Z.-M., "Volumetric Property Improvement for the Soave-Redlich-Kwong Equation of State," *Industrial & Engineering Chemistry Research*, Vol. 45, No. 5, 2006, pp. 1829-1839. https://doi.org/10.1021/ie051058v, URL https://pubs.acs.org/doi/full/10.1021/ie051058v

[28] Chung, T.-H., Ajlan, M., Lee, L.L., Starling, K.E., "Generalized Multiparameter Correlation for Nonpolar and Polar Fluid Transport Properties," *Industrial & Engineering Chemistry Research*, Vol. 27, No. 4, 1988, pp. 671-679. https://doi.org/10.1021/ie00076a024, URL https://pubs.acs.org/doi/10.1021/ie00076a024

[29] Hugill, J.A., van Welsenes, A.J., "Surface Tension: A Simple Correlation for Natural Gas + Condensate Systems," *Fluid Phase Equilibria*, Vol. 29, 1986, pp. 383-390. https://doi.org/10.1016/0378-3812(86)85038-5, URL https://www.sciencedirect.com/science/article/pii/0378381286850385\

[30] Soave, G., Gamba, S., Pellegrini, L.A., "SRK Equation of State: Predicting Binary Interaction Parameters of Hydrocarbons and Related Compounds," *Fluid Phase Equilibria*, Vol. 299, No. 2, 2010, pp. 285-293. https://doi.org/10.1016/j.fluid.2010.09.012, URL https://www.sciencedirect.com/science/article/pii/S037838121000467X

[31] Nannoolal, Y., Rarey, J., Ramjugernath, D., "Estimation of Pure Component Properties. Part 2. Estimation of Critical Property Data by Group Contribution," *Fluid Phase Equilibria*, Vol. 252, No. 1-2, 2007, pp. 1-27. https://doi.org/10.1016/j.fluid.2006.11.014, URL https://www.sciencedirect.com/science/article/pii/S0378381206004985

[32] Tahami, S., Ghasemitabar, H., Movagharnejad, K., "Estimation of the Acentric Factor of Organic Compounds Via a New Group Contribution Method," *Fluid Phase Equilibria*, Vol. 499, 2019, pp. 112246. https://doi.org/10.1016/j.fluid.2019.112246, URL https://www.sciencedirect.com/science/article/pii/S0378381219302997

[33] Passut, C.A., Danner, R.P., "Correlation of Ideal Gas Enthalpy, Heat Capacity, and Entropy," *Industrial & Engineering Chemistry Process Design and Development*, Vol. 11, No. 4, 1972, pp. 543-546. https://doi.org/10.1021/i260044a016, URL https://pubs.acs.org/doi/10.1021/i260044a016

[34] Joback, K.G., Reid, R.C., "Estimation of Pure-Component Properties from Group-Contributions," *Chemical Engineering Communications*, Vol. 57, No. 1-6, 1987, pp. 233-243. https://doi.org/10.1080/00986448708960487, URL https://www.tandfonline.com/doi/abs/10.1080/00986448708960487

[35] Davis, B.W., Poblador-Ibanez, J., Sirignano, W.A., "Two-Phase Developing Laminar Mixing Layer at Supercritical Pressures," *International Journal of Heat and Mass Transfer*, Vol. 167, 2021, pp. 120687. https://doi.org/10.1016/j.ijheatmasstransfer.2020.120687, URL https://www.sciencedirect.com/science/article/pii/S0017931020336231

[36] Escalpez, L., Ma, P.C., Mayhew, E., Xu, R., Stouffer, S., Lee, T., Wang, H., Ihme, M., "Fuel Effects on Lean Blow-Out in a Realistic Gas Turbine Combustor," *Combustion and Flame*, Vol. 181, 2017, pp. 82-99. https://doi.org/10.1016/j.combustflame.2017.02.035, URL https://www.sciencedirect.com/science/article/pii/S0010218017300822

[37] Pickett, L.M., Manin, J., Di Sabatino, F., Nguyen, T., Kook, S., "Mimicking Gas-Turbine Spray Combustion in a Constant-Volume Premixed Combustion Vessel," *AIAA SCITECH 2023 Forum*, American Institute of Aeronautics and Astronautics, National Harbor, MD, 2023. https://doi.org/10.2514/6.2023-2049, URL https://arc.aiaa.org/doi/abs/10.2514/6.2023-2049

[38] Bokhart, A.J., Shin, D., Gejji, R., Buschhagen, T., Naik, S.V., Lucht, R.P., Gore, J.P., Sojka, P.E., Meyer, S.E., "Spray Measurements at Elevated Pressures and Temperatures Using Phase Doppler Anemometry," *55th AIAA Aerospace Science Meeting*, American Institute of Aeronautics and Astronautics, Grapevine, TX, 2017. https://doi.org/10.2514/6.2017-0828, URL https://arc.aiaa.org/doi/abs/10.2514/6.2017-0828

[39] Bokhart, A.J., Shin, D., Rodrigues, N.S., Sojka, P.E., Gore, J.P., Lucht, R.P., "Spray Characteristics of a Hybrid Airblast Pressure-Swirl Atomizer at Near Lean Blowout Conditions using Phase Doppler Anemometry," *2018 AIAA Aerospace Sciences Meeting*, American Institute of Aeronautics and Astronautics, Kissimmee, FL, 2018. https://doi.org/10.2514/6.2018-2187, URL https://arc.aiaa.org/doi/abs/10.2514/6.2018-2187

[40] Dafsari, R.A., Lee, H.J., Han, J., Park, D.-C., Lee, J., "Viscosity Effect on the Pressure Swirl Atomization of an Alternative Aviation Fuel," *Fuel*, Vol. 240, 2019, pp. 179-191. https://doi.org/10.1016/j.fuel.2018.11.132, URL https://www.sciencedirect.com/science/article/pii/S0016236118320283
[41] Vankeswaram, S.K., Sakthikumar, R., Deivandren, S., Hu, J.D.C., "Evaluation of Spray Characteristics of Aviation Biofuels and Jet A-1 from a Hybrid Airblast Atomizer," *Experimental Thermal and Fluid Science*, Vol. 142, 2023, pp. 110820. https://doi.org/10.1016/j.expthermflusci.2022.110820, URL https://www.sciencedirect.com/science/article/pii/S0894177722002163
[42] Poblador-Ibanez, J., Sirignano, W.A., "Temporal Atomization of a Transcritical Liquid n-decane Jet into Oxygen," *International Journal of Multiphase Flow*, Vol. 153, 2022, pp. 104130. https://doi.org/10.1016/j.ijmultiphaseflow.2022.104130, URL https://www.sciencedirect.com/science/article/pii/S0301932222001276
[43] Shin, D., Bokhart, A.J., Rodrigues, N.S., Sojka, P.E., Gore, J.P., Lucht, R.P., "Experimental Study of Spray Characteristics at Cold Start and Elevated Ambient Pressure using Hybrid Airblast Pressure-Swirl Atomizer," *AIAA SCITECH 2019 Forum*, American Institute of Aeronautics and Astronautics, San Diego, CA, 2019. https://doi.org/10.2514/6.2019-1737, URL https://arc.aiaa.org/doi/abs/10.2514/6.2019-1737
[44] Richter, S., Kukkadapu, G., Westbrook, C.K., Braun-Unkhoff, M., Naumann, C., Köhler, M., Riedel, U., "A Combined Experimental and Modeling Study of Combustion Properties of an Isoparaffinic Alcohol-to-Jet Fuel," *Combustion and Flame*, Vol. 240, 2022, pp. 111994. https://doi.org/10.1016/j.combustflame.2022.111994, URL https://www.sciencedirect.com/science/article/pii/S001021802200013X
[45] Luning Prak, D.J., Jones, M.H., Trulove, P., McDaniel, A.M., Dickerson, T., Cowart, J.S., "Physical and Chemical Analysis of Alcohol-to-Jet (ATJ) Fuel and Development of Surrogate Fuel Mixtures," *Energy & Fuels*, Vol. 29, No. 6, 2015, pp. 3760-3769. https://doi.org/10.1021/acs.energyfuels.5b00668, URL https://doi.org/10.1021/acs.energyfuels.5b00668
[46] Guzman, J., Kukkadapu, G., Brezinsky, K., Westbrook, C.K., "Experimental and Modeling Study of the Pyrolysis and Oxidation of an Iso-Paraffinic Alcohol-to-Jet Fuel," *Combustion and Flame*, Vol. 201, 2019, pp. 57-64. https://doi.org/10.1016/j.combustflame.2018.12.013, URL https://www.sciencedirect.com/science/article/pii/S0010218018305303
[47] Rachford Jr., H.H., Rice, J.D., "Procedure for Use of Electronic Digital Computers in Calculating Flash Vaporization Hydrocarbon Equilibrium," *Journal of Petroleum Technology*, Vol. 4, No. 10, 1952, pp. 19. https://doi.org/10.2118/952327-G, URL https://onepetro.org/JPT/article/4/10/19/162083/Procedure-for-Use-of-Electronic-Digital-Computers
[48] Michelsen, M.L., Heidemann, R.A., "Calculation of Critical Points from Cubic Two-Constant Equations of State," *AIChE Journal*, Vol. 27, No. 3, 1981, pp. 521-523. https://doi.org/10.1002/aic.690270326, URL https://aiche.onlinelibrary.wiley.com/doi/abs/10.1002/aic.690270326
[49] Yu, J., Eser, S., "Determination of Critical Properties (Tc, Pc) of Some Jet Fuels," *Industrial & Engineering Chemistry Research*, Vol. 34, No. 1, 1995, pp. 404-409. https://doi.org/10.1021/ie00040a045, URL https://pubs.acs.org/doi/10.1021/ie00040a045
[50] Nomura, H., Ujiie, Y., Rath, H.J., Sato, J., Kono, M., "Experimental Study on High-Pressure Droplet Evaporation Using Microgravity Conditions," *26th Symposium (International) on Combustion*, The Combustion Institute, Vol. 26, No. 1, 1996, pp. 1267-1273. https://doi.org/10.1016/S0082-0784(96)80344-4, URL https://www.sciencedirect.com/science/article/pii/S0082078496803444
[51] Zhang, H., "Evaporation of a suspended droplet in forced convective high-pressure environments," *Combustion Science and Technology*, Vol. 175, No. 12, 2003, pp. 2237-2268. https://doi.org/10.1080/714923282, URL https://doi.org/10.1080/714923282